Beam shaping in high-energy kW-class laser system Bivoj at HiLASE facility

Tomáš Paliesek[1,2], Petr Navrátil[1], Jan Pilař[1], Martin Divoký[1], Martin Smrž[1], and Tomáš Mocek[1]

[1]*HiLASE Center, Institute of Physics of the Czech Academy of Sciences, Za Radnici 828, 252 41 Dolni Brezany, Czech Republic*
[2]*Faculty of Nuclear Science and Physical Engineering, Czech Technical University in Prague, Břehová 7, 115 19 Prague, Czech Republic*

Abstract
A fully automatic fail-safe beam shaping system based on a liquid crystal on silicon spatial light modulator has been implemented in the high-energy kilowatt-average-power nanosecond laser system Bivoj. The shaping system corrects for gain nonuniformity and wavefront aberrations of the front-end of the system. The beam intensity profile and the wavefront at the output of the front end were successfully improved by shaping. The beam homogeneity defined by the beam quality parameters was improved 2-3 times. The RMS value of the wavefront was improved more than 10 times. Consequently, the shaped beam from the second preamplifier led to improvement of the beam profile at the output of the first main cryo-amplifier. The shaping system is also capable of creating nonordinary beam shapes, imprinting cross references into the beam, or masking certain parts of the beam.

Keywords: Beam shaping, wavefront shaping, LCoS SLM, high-energy laser, high-average-power laser

1. Introduction

High-average-power and high-energy lasers play an important role in many fields of current scientific research and industrial processing[8,12,26]. Due to the high energies in a pulse, large-aperture amplifiers are necessary. However, the amplification of a large aperture high-power high-energy laser beam in multistage amplifier systems often suffers from beam profile inhomogeneities caused by a nonuniform gain[14,29]. There is great effort to either precompensate or improve the spatial beam profile or wavefront in order to avoid optics damage in the amplifiers and to achieve the most uniform output. For this purpose, various types of spatial light modulator-based beam shapers have been deployed at several laser facilities in their laser systems[2,4,7,18,19,28] or in test experiments[3,5,20,22].

Spatial light modulators (SLM) allow to shape the incident beam and are used in various configurations. If the SLM is placed between crossed polarizers, each pixel can vary attenuation by rotating linear polarization between the polarizers[18,19]. There are also techniques based on computer generated holograms[22], optically-addressable transmissive light valves[2] or binary beam shapers using error diffusion[17,20]. Probably the most used are the methods that incorporate diffraction gratings and spatial filter for removing the unwanted diffraction orders. This principle allows to diffract away the unwanted energy by locally changing the diffraction efficiency of the phase mask. With appropriate SLM, the wavefront of the diffracted beam can also be shaped simultaneously and independently from the intensity profile with a single phase-only modulator.

The shaping system based on SLM and binary grating was demonstrated in several papers[3,5,7] and provided both high-resolution intensity and wavefront shaping. In these systems, the unwanted energy is diffracted away and filtered out. This can be potentially dangerous for the laser system and subsequent amplifiers when SLM suffers malfunction and reflects a higher amount of energy or creates a strange pattern in the reflected beam. Therefore, the stepped diffraction grating can be used instead of binary, allowing the shaped beam to be in the first diffraction order. This ensures the safety of shaping system when SLM malfunctions – nothing propagates through the spatial filter into the laser system. The technique was first introduced in[10] and discussed in[4] as a method suitable for laser beam shaping in high-energy systems with fail-safe feature and higher contrast, but it has never been deployed in any laser system, nor has it been used for the wavefront precompensation in such a system.

Correspondence to: T. Paliesek, Centrum HiLASE, Za Radnici 828, 252 41 Dolni Brezany, Czech Republic. Email: tomas.paliesek@hilase.cz

This peer-reviewed article has been accepted for publication but not yet copyedited or typeset, and so may be subject to change during the production process. The article is considered published and may be cited using its DOI.

This is an Open Access article, distributed under the terms of the Creative Commons Attribution licence (https://creativecommons.org/licenses/by/4.0/), which permits unrestricted re-use, distribution, and reproduction in any medium, provided the original work is properly cited.

10.1017/hpl.2023.79

https://doi.org/10.1017/hpl.2023.79 Published online by Cambridge University Press

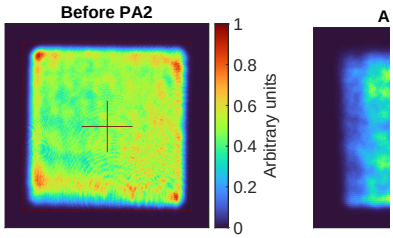

Figure 1: Beam profile degradatic nonuniformity in the second pre-amplif

In this article, we therefore introc our knowledge, the first implementati grammable beam shaping system base on silicon (LCoS) SLM into the high- energy laser. The shaping system c nonuniformity in the second preamplif system with fully automatic operatior rithm based only on the feedback from wavefront sensor. Moreover, the shapir

- simultaneously precompensate w the beam gets while being amplifi
- create nonordinary beam shapes th output capabilities and applicatior
- imprint cross reference, hole or otl ment of the optics or mask certai needed.

1.1. Motivation

The laser beam from the Bivoj laser LASE research center (Dolni Brezar is used mainly for applications such ing (LSP)[1,25] and laser-induced dam (LIDT)[9]. Both applications require a laser beam. However, during the proc the beam experiences wavefront, inter distribution degradation in various stag fier chain.

The main sources of wavefront aberrations were identified as static aberrations of optical elements and thermal aberrations of gain media. Other sources of aberration have random character (turbulent flow of the coolant gas inside the multi-slab chamber, vibrations, air turbulences in the beam path) and are not significant in magnitude. Adaptive optics systems are used in both main multi-pass multi-slab cryoamplifiers to correct for these aberrations[24].

The polarization changes originate from stress-induced birefringence caused by heat load in the amplifier head. As a result, it reduces the energy available to polarization-sensitive experiments or ddegrades the beam profile when the beam passes through any diattenuator. These polarization changes were mitigated by injecting optimized polarization into the amplifier[27].

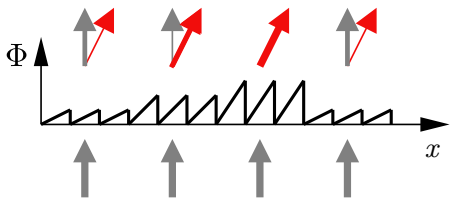

Figure 2: Principle of the beam shaping with SPs. Each triangle represents one blazed (stepped) grating and according to the maximum phase modulation Φ it diffracts a certain amount of energy to the first diffraction order. Diffraction to other orders is neglected for clarity.

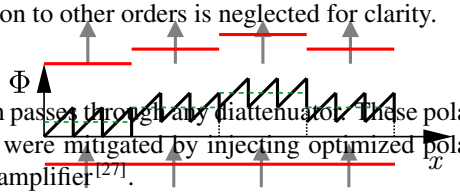

Due to the nonuniform gain distribution in the second pre-amplifier (pump source is not uniform), the intensity distribution gets distorted (see Fig. 1) and this distortion may be delivered to the output of the laser system according to the application-required output energy.

The SLM can not only smoothen the beam for various output energies, but it allows amplification of nonordinary beam shapes that could open up new application opportunities for Bivoj laser system. For example in material processing applications or as an OPCPA pump source where the frequency doubled[23] circular flat-top beam is needed. The annular intensity distribution might be interesting in applications where temperature is the key parameter, for example laser heat treatment or laser hardening[15] or it can be used to improve deposition process symmetry in direct annular laser beam based metal deposition[16].

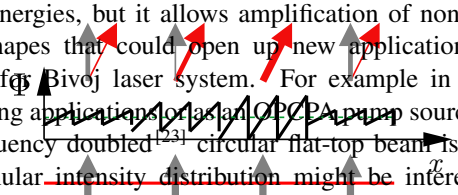

2. Beam and wavefront shaping principle

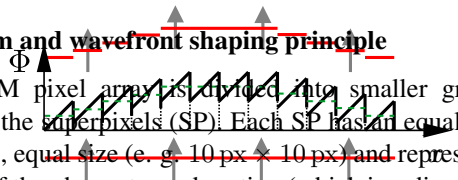

The SLM pixel array is divided into smaller groups of pixels – the superpixels (SP). Each SP has an equal number of pixels, equal size (e. g. 10 px × 10 px) and represents one period of the phase stepped grating (which is a discrete form of the blazed diffraction grating). The diffraction efficiency of each SP is adjustable as shown in Fig. 2 and can be as high as 71 % (see Fig. 9). By this approach, we spatially control the amount of incident power diffracted in the first diffraction order, and only this order passes through the spatial filter in the relay imaging telescope after the SLM.

With this method, a failsafe operation of the beam shaping system is guaranteed (Fig. 3) as the probability that the failure creates a diffraction grating with a grating period that diffracts the beam through the spatial filter is low. In case of SLM failure, nothing is diffracted into the amplifier chain unlike in[5,7] where the unnecessary energy is removed by diffraction and in case of SLM failure, some energy may still propagate into an amplifier chain. The safe operation

https://doi.org/10.1017/hpl.2023.79 Published online by Cambridge University Press

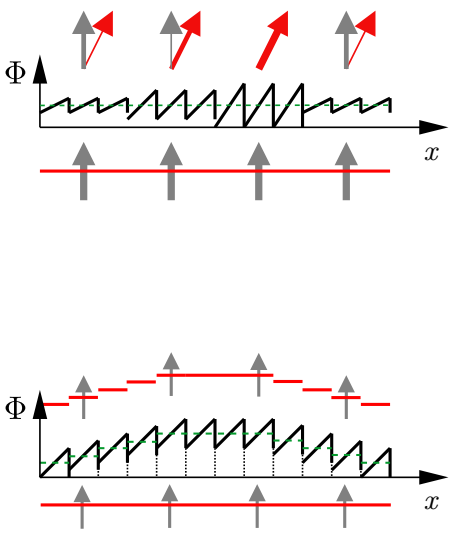

Figure 4: Principle of the wavefront shaping with SPs. Each SP represents one blazed (stepped) grating, and according to the individual constant phase shift, each SP adds a spatially distributed phase delay. The principle is explained on the zero-th diffraction order and diffraction to other orders is neglected for clarity.

of the beam shaping system is additionally provided by the software control discussed in Sec. 4.1.

The diffraction efficiency of each SP is given by the intensity transmittance function (ITF) defined as follows:

$$\mathrm{ITF} = \frac{\text{reference profile}}{\text{incident profile}}, \tag{1}$$

where the incident profile is the intensity distribution of the laser beam right before the SLM and the reference profile is the desired intensity distribution right after the SLM in the first diffraction order.

The reference intensity profile was decided to be the square super-Gaussian beam according to Eq. (2) with $n = 4$:

$$\mathrm{RF} = A \cdot \exp\left\{ -\left[\left(\frac{x - c_x}{h}\right)^{2n} + \left(\frac{y - c_y}{h}\right)^{2n}\right]\right\}, \tag{2}$$

where RF is reference profile, A is the amplitude, x, y are the horizontal and vertical coordinates, c_x, c_y are the beam center coordinates, h controls the beam width and n is the order of the super-Gaussian function.

While the required pixel phase range of SLM for the above-explained shaping is 2π rad and the phase range of our SLM is 4.6π rad, the rest can be used for the shaping of the wavefront of the incident beam. The principle is to add a constant phase shift to each SP individually, as can be seen from Fig. 4. Therefore, the maximum peak-to-valley value of wavefront modulation added by SLM is $1.3\,\lambda$. Similarly to the intensity transmittance function, the phase transmittance

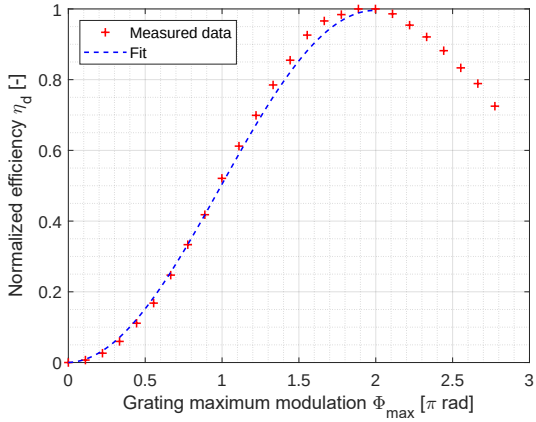

Figure 5: Normalized diffraction efficiency response of the stepped grating as a function of the maximum phase modulation Φ_{max}. Measured data are fit with Eq. (4).

function (PTF) is computed from the reference wavefront and incident wavefront:

$$\mathrm{PTF} = \text{reference wavefront} - \text{incident wavefront}, \tag{3}$$

and obtained function gives the constant phase modulation (in λ) for each SP that can be directly displayed on SLM without any conversion.

2.1. *SLM and camera spatial registration*

The beam shaping based on the ITF can only work with exact information of location of the beam on the SLM. During the process of spatial calibration, spots with no intensity (holes), Gaussian edge profile, and well-defined positions are created by the SLM in the beam and captured by the near-field camera. The location of each hole in the camera image is then detected, and together with the information about location of holes on the SLM, a spatial transformation is obtained. A similar technique was used in[7,28]. The beam captured by the camera and transformed by spatial transformation is then considered as the incident beam in the ITF calculation.

2.2. *Intensity calibration*

The intensity calibration indicates the diffraction efficiency response as a function of the maximum phase depth of the stepped grating as in Fig. 5. Even though, the analytic expression is in the form of sinc^2 function, the measured data are fit with:

$$\eta_d(\Phi_{\mathrm{max}}) = a \cdot \sin\left(b\Phi_{\mathrm{max}} - c\right) + a, \tag{4}$$

which is easily invertible on $\langle 0, 2\pi \rangle$ in order to find maximum phase modulation for required diffraction efficiency given by the ITF. Also, there is no need to know the exact

https://doi.org/10.1017/hpl.2023.79 Published online by Cambridge University Press

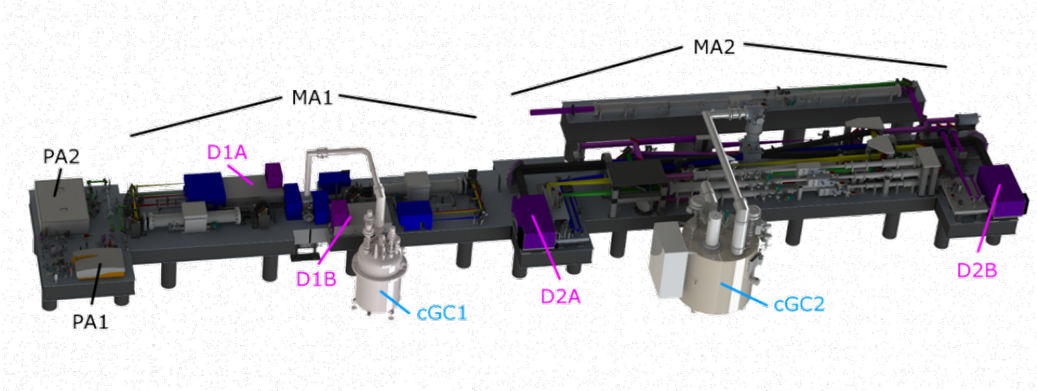

Figure 6: Laser system Bivoj model. PA - room temperature preamplifiers, MA - main cryoamplifiers, D - diode pumping modules, cGC - cryogenic gas coolers. Source[11].

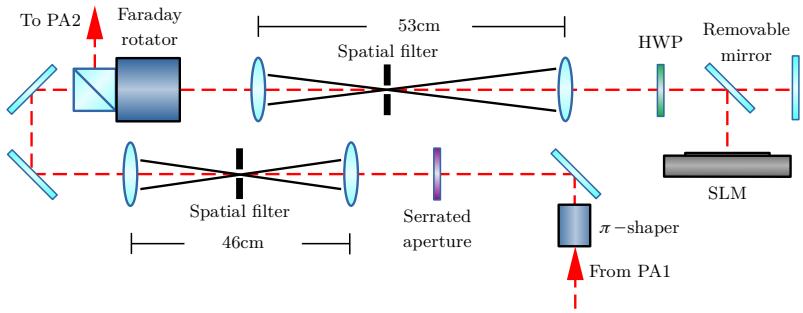

Figure 7: Scheme of the front-end beam shaping section of Bivoj laser system.

diffraction efficiency response due to the iterative shaping algorithm (see Sec. 4.1). Our SLM has 4.6π rad phase range and only 0–2π rad span is used for intensity shaping. The rest of the SLM's phase range is utilized for wavefront shaping.

3. Bivoj laser system

The Bivoj laser system (Fig. 6) is a multi-slab high-energy nanosecond diode pumped solid state laser with high-average power[6,21]. Recently, a 150 J operation at 10 Hz repetition rate and 10 ns pulse length was achieved[13]. The system consists of three main sections, which are: front-end (FE) with two preamplifiers (PA1, PA2) and two main power cryoamplifiers (MA1, MA2), as Fig. 6 shows. Fig. 1 represents the beam intensity profile in the second preamplifier (PA2) in FE that degraded due to the nonuniform gain. PA2 increases the pulse energy up to 50 mJ.

After the PA2, the first main cryoamplifier (MA1) increases pulse energy up to 14 J and tends to smooth the beam intensity profile because the cryo-cooled active Yb:YAG slabs are working in saturation. This is observed especially at higher output pulse energies. A wide range of beam users and applications also require lower pulse energies (e.g. around ∼2 J) when the beam profile is not smoothed in MA1.

3.1. SLM deployment

The beam shaping system was implemented into the front-end of the Bivoj laser system. The front-end begins with a cw fiber oscillator. The cw beam is then shaped in the temporal domain by an acousto-optic modulator, amplified in a fiber amplifier and finally shaped in the temporal domain again by an electro-optic modulator. Pulses with arbitrary shape and pulse duration of 2–14 ns are generated with the output energy of 10 nJ for a 10 ns pulse. The pulses are then amplified by the regenerative amplifier (PA1) based on the Yb:CaF_2 rod to ∼4 mJ with the repetition rate of 10 Hz. After PA1, the 2 mm Gaussian beam is spatially shaped to 8 mm × 8 mm square with the super-Gaussian profile in the beam shaper consisting of the expanding telescope, the π-shaper and the serrated aperture with the spatial filter.

After the shaping, the beam passes through the polarization beam splitter and the Faraday rotator and is relay-imaged onto the SLM by the spatial filtering telescope. Finally, a half-wave plate (HWP) is used to adjust polarization before the SLM (Fig. 7). The SLM (model X13138-03 by Hamamatsu) has 1272 px × 1024 px resolution, 12.5 µm pixel pitch, 96 % fill factor, and 15.8 mm × 12.8 mm ac-

https://doi.org/10.1017/hpl.2023.79 Published online by Cambridge University Press

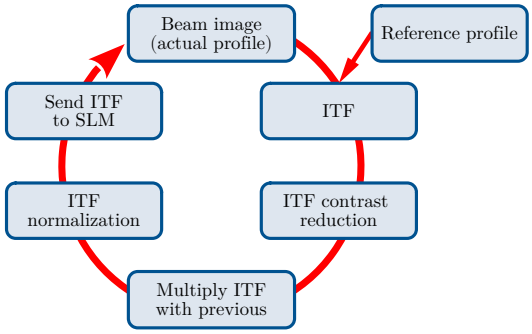

Figure 8: Iterative shaping algorithm schematics. At the beginning of the iteration, the ITF is obtained from the actual and reference beam profiles. Then, the contrast of the ITF is reduced, it is multiplied with the previous ITF, normalized and send to the SLM.

tive area size. The maximum phase modulation is around $4.6\pi\,\mathrm{rad}$ with $12\,\mathrm{bit}$ driving signal. The SLM is adjusted in a way that only the first diffraction order passes through the pinhole of the spatial filter on its way back to the Faraday rotator. This ensures the safety of the system in case of SLM failure. The telescope before the SLM also modifies the beam size ($\sim 11\,\mathrm{mm} \times 11\,\mathrm{mm}$) according to the SLM active area size.

After the telescope, the beam passes through the Faraday rotator and is reflected by the polarization beam splitter to the second pre-amplifier (PA2) where pulses are amplified to the energy of $\sim 50\,\mathrm{mJ}$. The PA2 is an 8-pass amplifier based on Yb:YAG and preserves the square super-Gaussian beam profile, which is subsequently expanded to $21\,\mathrm{mm} \times 21\,\mathrm{mm}$ and injected into the $10\,\mathrm{J}$ main cryoamplifier. A detailed description of the main cryoamplifiers and the overall system can be found in[12]. The SLM was implemented into the system using a removable mirror that, if removed, allows the system to operate without the SLM. The near-field feedback camera is located after PA2 in the SLM relay-image plane.

4. PA2 nonuniform gain correction

4.1. Closed loop operation

The shaping algorithm is based on a feedback from the near-field camera that was placed after the PA2. In this configuration, when the pulses are amplified in the PA2, the shaping loop must also take into account the dynamic processes in the amplifier itself (such as intensity saturation) and the inaccuracy of the grating efficiency curve (Fig. 5). We therefore correct the beam intensity profile deformations in an iterative way, when in each iteration only a partial correction is applied. The feedback camera, SLM and PA2 gain medium are relay-imaged one to each other.

The diagram of the shaping algorithm is in Fig. 8. It is based on the ITF but in each iteration, only a small portion of the ITF is applied. This is represented as the ITF contrast reduction according to the equation:

$$\overline{\mathrm{T}} = k \cdot \left[\mathrm{T} - m\right] + m, \tag{5}$$

where k is the coefficient of the iterative algorithm, T is the matrix representing calculated intensity transmittance function for each SP, m is the average value of T matrix and $\overline{\mathrm{T}}$ is the ITF with reduced contrast. This ensures correction of inaccuracies in the efficiency response curve. The coefficient of the iterative algorithm k influences the quality and speed of shaping and is determined by a user. After the contrast reduction, the ITF is multiplied with the one from the previous iteration and normalized to 1. The control algorithm monitors the beam after each iterration for intensity spikes before proceeding to next iterration to avoid potential damage in the laser system.

4.2. Beam quality coefficients and shaping efficiency

The quality of the beam intensity profile is described with beam quality coefficients (BQC) - intensity contrast and deviation from the reference profile. The first describes only quality of the beam plateau and the second one characterizes the beam intensity distribution as a whole.

Intensity contrast – indicates the uniformity of the beam plateau:

$$\mathrm{IC} = \frac{I_{max} - I_{min}}{I_{max} + I_{min}}, \tag{6}$$

where I_{max} and I_{min} correspond to the maximum and minimum average pixel intensity measured over any area within the plateau region equivalent to 10^{-4} of the plateau area.

Deviation from reference profile – is defined as a quadratic deviation:

$$\mathrm{DRP} = \sqrt{\frac{1}{N-1}\sum_{i=1}^{N}(I_i - \overline{I}_i)^2}, \tag{7}$$

where I_i is the intensity of i-th pixel in the beam image and $\overline{I}_i$ is the intensity of i-th reference pixel in the reference beam profile.

Shaping efficiency – is another important characteristic of the shaping system. Two factors impact shaping efficiency η according to:

$$\eta = \eta_s \cdot \eta_d, \tag{8}$$

where η_s is the efficiency of the shaping algorithm and η_d is the diffraction efficiency of the used stepped diffraction grating that depends on the grating period ξ as Fig. 9 shows. According to this plot, the grating period for the shaping experiments is chosen to either maintain maximum diffraction efficiency η_d or to get better shaping resolution (discussed in the next section). The efficiency of the shaping

https://doi.org/10.1017/hpl.2023.79 Published online by Cambridge University Press

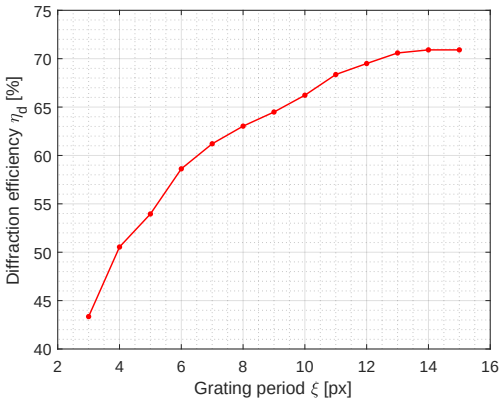

Figure 9: Maximum diffraction efficiency as a function of the stepped grating period ξ. The higher the number of pixels is in SP, the more converges the phase stepped profile to the blazed one, which has the maximum diffraction efficiency of $100\,\%$ in the first diffraction order.

algorithm η_s is caused by the removal of unwanted energy from the beam profile.

4.3. PA2 output correction results

The beam shaping loop was tested by shaping the beam before the PA2 to optimize its output beam. Before each shaping run, the camera background was removed by capturing image with no diffraction on the SLM and subtracted from every subsequently captured image.

Fig. 10 shows the beam intensity profile at the output of the PA2 before and after the shaping run. The coefficient of iterative algorithm was set to $k = 0.1$. The beam quality coefficients were calculated for each iteration and are plotted in Fig. 11. As can be seen from the same figure, after 11 iterations, both beam quality coefficients reached values less than one-half of their initial values. After 25 iterations, the beam closely matches the desired reference profile (Fig. 10) and in subsequent iterations, its profile and beam quality coefficients oscillate around constant values.

The shaping efficiency was also measured (Fig. 11). The stepped diffraction grating with $14\,\mathrm{px}$ SP was used. Smaller sizes of SP did not improve shaping performance, so the SP with maximum possible diffraction efficiency η_d was chosen. Therefore, the overall efficiency η after 25 iterations was around $39\,\%$ according to the plot in Fig. 9. It should be noted that the designed PA2 output energy is $100\,\mathrm{mJ}$, which is considerably higher than what is actually needed, and the energy losses by shaping can be easily restored by adjusting its output power.

The long-time operation was tested subsequently. At the beginning of the day, the beam was shaped by the iterative algorithm after the laser was thermally stabilized. The beam quality coefficients were tracked during the six-hour-long laser operation. The variations of IC and DRP were only

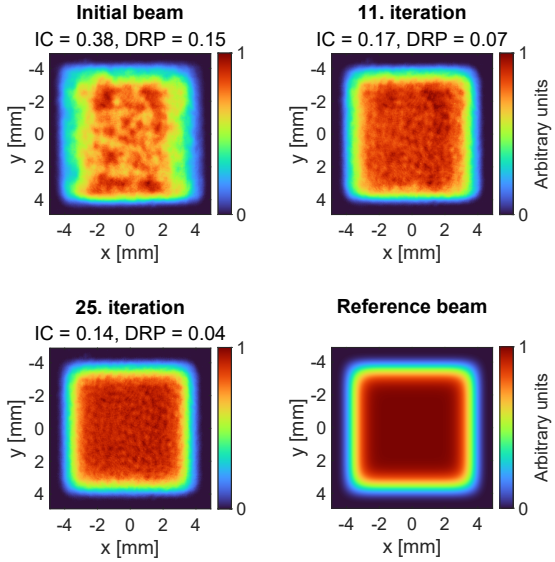

Figure 10: Output of the second pre-amplifier PA2 during shaping and reference beam profile.

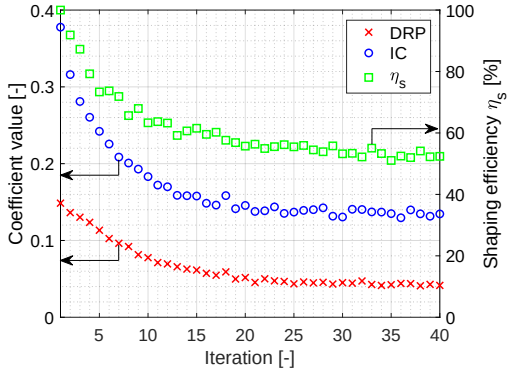

Figure 11: Beam quality coefficients and shaping efficiency during the shaping of the beam at the output of PA2.

minimal (DRP stayed the same and IC increased from 0.16 to 0.17) and did not have any impact on the laser system operation and so no other run of the shaping algorithm during that day was needed. This long-time operation characteristic is strongly dependent on the beam movement on the SLM. During normal operation, the beam moves significantly only at the start of the system, when all components need to reach thermal equilibrium (this takes around 45 minutes). The time necessary for the shaping operation to perform calibration routines and converge to the desired beam profile was less than a minute (in the $10\,\mathrm{Hz}$ laser regime).

The shaped beam was then injected into the first main cryoamplifier (MA1) and amplified first to the energy of $2\,\mathrm{J}$ and then to the energy of $6\,\mathrm{J}$. The results are shown in Fig. 12. At $2\,\mathrm{J}$ output energy, the smoothing of the beam plateau is more visible compared to the $6\,\mathrm{J}$ output, when the beam plateau is also smoothed by saturation of

https://doi.org/10.1017/hpl.2023.79 Published online by Cambridge University Press

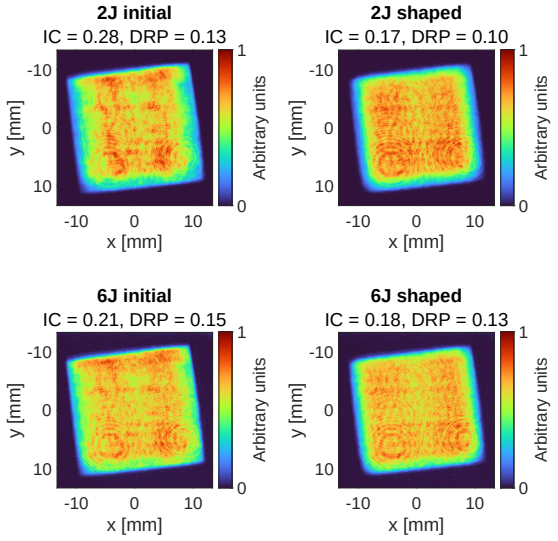

Figure 12: Comparison of outputs from the MA1 amplifier with and without shaping. The circular diffraction patterns in the images are caused by dust particles or defects in the diagnostic optical setup and are not present in the actual beam profile.

the amplification in MA1. But, on the other hand, the saturation of the amplification causes changes in the beam edge steepness (the closed-loop works with the feedback near-field camera at the end of the front-end, so it does not consider the effect of saturation of amplification in MA1). The pump beam is a square super-Guassian with $n = 32$ according to Eq. (2) and that is one of the reasons why the DRP coefficient value of the shaped beam increased after amplification in MA1 at 6 J output energy. The alignment of the amplifier can also result in uneven amplification of beam edges because each pass through the amplifier head is directed at a slightly different angle and might not be exactly overlapped with previous pass.

5. Wavefront pre-compensation

The wavefront shaping capabilities were tested on the shaped beam from the Fig. 10. The feedback wavefront sensor (Phasics SID4) was placed after the PA2 using a beamsplitter in the same SLM relay-imaged plane as the feedback near-field camera. The initial beam intensity profile distribution was first shaped by running a few iterations of the intensity shaping algorithm, and then the phase transmittance function based on the wavefront from the wavefront sensor was applied in 2 iterations. The wavefront data obtained from the wavefront sensor were spatially registered according to the beam edges, but the procedure introduced in Section 2.1 can also be used with this type of wavefront sensor. The results of aberration correction can be seen from Fig. 13. The initial wavefront RMS value was improved by more than 10x. The effect of wavefront shaping on the intensity distribution was negligible.

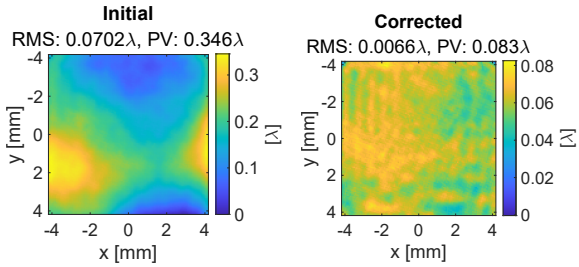

Figure 13: Aberration correction in front-end of the Bivoj laser system. Wavefronts measured with Phasics SID4 wavefront sensor at the output of the second pre-amplifier PA2 before and after correction.

5.1. MA1 aberration pre-compensation with SLM

The beam with corrected (flat) wavefront was then injected into MA1 amplifier and the wavefront at its output was measured. However, it was not improved significantly (in terms of RMS and PV values), only its shape was slightly different mainly because the front-end aberration magnitude is small compared to the overall aberration magnitude of MA1.

We also tried to enhance the performance of the MA1 adaptive optics system with SLM. The deformable mirror after 3rd pass in MA1 amplifier corrects thermally induced aberrations. It has 7×7 actuators, so it is not able to correct higher-frequency aberrations. The aim of this experiment was to precompensate these aberrations with SLM in the front-end and improve the output wavefront of MA1.

First, the wavefront at the front-end output was corrected and the same was done with DM in the MA1 amplifier. Then, the data from wavefront sensor at the output of MA1 was used to obtain a new PTF that was sent to SLM with previous PTFs. But this approach did not improve the MA1's output wavefront significantly (compared to solo MA1 adaptive optics system performance) mainly because the high-frequency aberrations in the MA1 were not static and were changing unpredictably (they are caused primarily by fast turbulent flow of the cooling helium).

6. Creating nonordinary beam shapes

The shaping system allows to diffract basically any beam shape that fits into the original unshaped beam. Most interesting are circular flat-top beams or annular (ring) beams, as was stated in the motivation section. These beam shapes were created with the closed-loop algorithm, injected into the Bivoj amplifier chain and amplified in both main amplifiers.

https://doi.org/10.1017/hpl.2023.79 Published online by Cambridge University Press

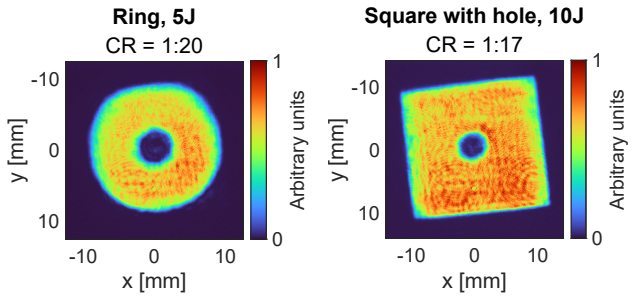

Figure 14: Nonordinary beam shapes at the output of MA1 amplifier (CR - contrast ratio).

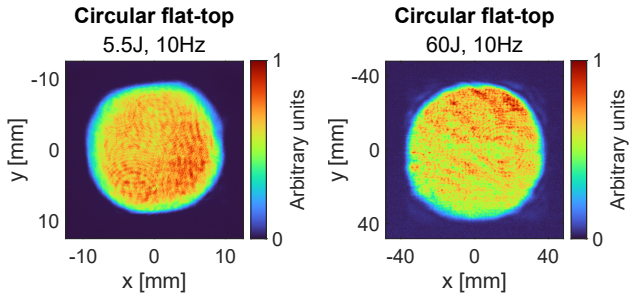

Figure 15: Circular flat-top beam at the output of MA1 and MA2 amplifier.

Some of the results can be seen in Fig. 14 and Fig. 15. The annular beam was created by subtracting 2 circular super-Gaussian profiles. The square super-Gaussian profile with a circular hole was generated similarly. The hole size was chosen randomly and is around $5\,\mathrm{mm}$ for the ring and $4\,\mathrm{mm}$ for the square shape. The contrast ratio (CR) was calculated as the ratio of average intensities in the hole area to the beam plateau. The separation edge of the hole area for the CR calculation was given by the intensity threshold of $5\,\%$.

The maximum achievable energy for these beam shapes is given by their area ratio to the original square beam, so the fluence inside the amplifiers is preserved. The theoretical energy limit for the inscribed circular beam amplified in the MA1 and MA2 amplifier is $78\,\%$ of the full square beam.

7. Conclusions

The problem with the nonuniform gain in the second pre-amplifier (PA2) of the Bivoj laser system was addressed by the development of the beam shaping system based only on the single LCoS spatial light modulator and the near-field CCD camera. The shaping system is fully automatic, fail-safe against SLM malfunction and is incorporated directly in the main laser control system.

The beam intensity profile at the output of PA2 was successfully improved by shaping. The beam homogeneity defined by the beam quality parameters was improved 2-3 times and the overall shaping efficiency of $39\,\%$ was reached. Consequently, the shaped beam from PA2 led to improvement of the beam profile at the output of the first main cryo-amplifier (MA1), especially at lower output energies.

The RMS of the PA2 output wavefront was improved more than 10 times by wavefront shaping. However, the wavefront precompensation in front-end had no significant effect on the output wavefront of the MA1 amplifier with its adaptive optics system.

The beam shaping system allowed to inject nonordinary beam shapes into the amplifier chain. Amplification of the circular flat-top beam in the 100J amplifier MA2 was successful, and therefore we conclude that tailoring kW-class output beam shapes is possible and the beam shape (among other output characteristics, such as pulse shape and length, energy and repetition rate) can be adjusted to fit the needs of individual experiments and potentially extend application range of the Bivoj laser system.

Moreover, the shaping system can imprint a cross reference or mask a certain part of the beam if needed.

Disclosures

The authors declare no conflicts of interest.

Data availability

Data underlying the results presented in this paper are not publicly available at this time but may be obtained from the authors upon reasonable request.

References

1. X. Arnoult, M. Böhm, J. Brajer, J. Kaufman, S. Zulić, D. Rostohar, and T. Mocek. HILASE center: development of new-generation lasers for laser shock peening. In J. Liu, M. Hong, and R. Xiao, editors, *Advanced Laser Processing and Manufacturing II*, page 31. SPIE, 2018.
2. A. A. S. Awwal, C. Orth, E. Tse, J. Matone, M. Paul, C. Hardy, G. Brunton, M. Hermann, S. Yang, J. M. M. DiNicola, M. Rever, S. Dixit, and J. Heebner. Image processing and control of a programmable spatial light modulator for spatial beam shaping. In A. A. S. Awwal, editor, *Proc. SPIE 8602*, page 86020A, 2013.
3. V. Bagnoud and J. D. Zuegel. Independent phase and amplitude control of a laser beam by use of a single-phase-only spatial light modulator. *Optics Letters*, 29(3):295, Feb. 2004.
4. S.-W. Bahk, I. Begishev, and J. Zuegel. Precompensation of gain nonuniformity in a Nd:glass amplifier using a programmable beam-shaping system. *Optics Communications*, 333:45–52, Dec. 2014.

https://doi.org/10.1017/hpl.2023.79 Published online by Cambridge University Press

5. S.-W. Bahk, E. Fess, B. E. Kruschwitz, and J. D. Zuegel. A high-resolution, adaptive beam-shaping system for high-power lasers. *Optics Express*, 18(9):9151, Apr. 2010.
6. S. Banerjee, P. D. Mason, K. Ertel, P. Jonathan Phillips, M. De Vido, O. Chekhlov, M. Divoky, J. Pilar, J. Smith, T. Butcher, A. Lintern, S. Tomlinson, W. Shaikh, C. Hooker, A. Lucianetti, C. Hernandez-Gomez, T. Mocek, C. Edwards, and J. L. Collier. 100 J-level nanosecond pulsed diode pumped solid state laser. *Optics Letters*, 41(9):2089, May 2016.
7. M. Barczys, S.-W. Bahk, M. Spilatro, D. Coppenbarger, E. Hill, T. H. Hinterman, R. W. Kidder, J. Puth, T. Touris, and J. D. Zuegel. Deployment of a spatial light modulator-based beam-shaping system on the OMEGA EP laser. In A. A. S. Awwal, editor, *Proc. SPIE 8602*, page 86020F, San Francisco, California, USA, Feb. 2013.
8. R. Betti and O. A. Hurricane. Inertial-confinement fusion with lasers. *Nature Physics*, 12(5):435–448, 2016.
9. P. Cech, J. Vanda, M.-G. Muresan, M. Mydlar, K. Pilna, and J. Brajer. Laser induced damage threshold testing at hilase. *MM Science Journal*, 2019(5):3657–3661, 2019.
10. J. A. Davis, D. M. Cottrell, J. Campos, M. J. Yzuel, and I. Moreno. Encoding amplitude information onto phase-only filters. *Applied Optics*, 38(23):5004, 1999.
11. M. Divoky, J. Pilar, M. Hanus, P. Navratil, M. Sawicka-Chyla, M. De Vido, P. J. Phillips, K. Ertel, T. Butcher, M. Fibrich, J. T. Green, M. Koselja, J. Preclikova, J. Kubat, J. Houzvicka, B. Rus, J. Collier, A. Lucianetti, and T. Mocek. Performance comparison of yb:yag ceramics and crystal gain material in a large-area, high-energy, high average–power diode-pumped laser. *Optics Express*, 28(3):3636, 2020.
12. M. Divoky, M. Smrz, M. Chyla, P. Sikocinski, P. Severova, O. Novak, J. Huynh, S. Nagisetty, T. Miura, J. Pilař, O. Slezak, M. Sawicka, V. Jambunathan, J. Vanda, A. Endo, A. Lucianetti, D. Rostohar, P. Mason, P. Phillips, K. Ertel, S. Banerjee, C. Hernandez-Gomez, J. Collier, and T. Mocek. Overview of the HiLASE project: high average power pulsed DPSSL systems for research and industry. *High Power Laser Science and Engineering*, 2:e14, May 2014.
13. M. Divoký, J. Pilař, M. Hanuš, P. Navrátil, O. Denk, P. Severová, P. Mason, T. Butcher, S. Banerjee, M. De Vido, C. Edwards, J. Collier, M. Smrž, and T. Mocek. 150 J DPSSL operating at 1,5 kW level. *Optics Letters*, 46(22):5771, Nov. 2021.
14. C. Dorrer and J. D. Zuegel. Design and analysis of binary beam shapers using error diffusion. *Journal of the Optical Society of America B*, 24(6):1268, 2007.
15. M. Duocastella and C. Arnold. Bessel and annular beams for materials processing. *Laser & Photonics Reviews*, 6(5):607–621, Sept. 2012.
16. E. Govekar, A. Jeromen, A. Kuznetsov, M. Kotar, and M. Kondo. Annular laser beam based direct metal deposition. *Procedia CIRP*, 74:222–227, 2018.
17. S. Li, L. Ding, P. Du, Z. Lu, Y. Wang, L. Zhou, and X. Yan. Using the spatial light modulator as a binary optical element: application to spatial beam shaping for high-power lasers. *Applied Optics*, 57(24):7060, 2018.
18. S. Li, Z. Lu, P. Du, Y. Wang, L. Ding, and X. Yan. Beam shaping by using small-aperture SLM and DM in a high power laser. In S. Zhuang, J. Chu, and J.-W. Pan, editors, *Young Scientists Forum 2017*, page 130. SPIE, 2018.
19. S. Li, Y. Wang, Z. Lu, L. Ding, P. Du, Y. Chen, Z. Zheng, D. Ba, Y. Dong, H. Yuan, Z. Bai, Z. Liu, and C. Cui. High-quality near-field beam achieved in a high-power laser based on SLM adaptive beam-shaping system. *Optics Express*, 23(2):681, Jan. 2015.
20. J. Liang, R. N. Kohn, Jr., M. F. Becker, and D. J. Heinzen. High-precision laser beam shaping using a binary-amplitude spatial light modulator. *Applied Optics*, 49(8):1323, 2010.
21. P. Mason, M. Divoký, K. Ertel, J. Pilař, T. Butcher, M. Hanuš, S. Banerjee, J. Phillips, J. Smith, M. De Vido, A. Lucianetti, C. Hernandez-Gomez, C. Edwards, T. Mocek, and J. Collier. Kilowatt average power 100 J-level diode pumped solid state laser. *Optica*, 4(4):438, Apr. 2017.
22. J. M. Maxson, A. C. Bartnik, and I. V. Bazarov. Efficient and accurate laser shaping with liquid crystal spatial light modulators. *Applied Physics Letters*, 105(17):171109, 2014.
23. J. P. Phillips, S. Banerjee, P. Mason, J. Smith, J. Spear, M. De Vido, K. Ertel, T. Butcher, G. Quinn, D. Clarke, C. Edwards, C. Hernandez-Gomez, and J. Collier. Second and third harmonic conversion of a kilowatt average power, 100-J-level diode pumped Yb:YAG laser in large aperture LBO. *Optics Letters*, 46(8):1808, Apr. 2021.
24. J. Pilar, O. Slezak, P. Sikocinski, M. Divoky, M. Sawicka, S. Bonora, A. Lucianetti, T. Mocek, and H. Jelinkova. Design and optimization of an adaptive optics system for a high-average-power multi-slab laser (HiLASE). *Applied Optics*, 53(15):3255, May 2014.
25. D. Rostohar, J. Koerner, R. Boedefeld, A. Lucianetti, and T. Mocek. How new laser development can help laser shock peening penetration to widen industrial applications? In *2017 IEEE 3rd International Forum on Research and Technologies for Society and Industry (RTSI)*, pages 1–4. IEEE, 2017.
26. B. Rus, P. Bakule, D. Kramer, J. Naylon, J. Thoma, M. Fibrich, J. T. Green, J. C. Lagron, R. Antipenkov, J. Bartoníček, F. Batysta, R. Baše, R. Boge, S. Buck,

https://doi.org/10.1017/hpl.2023.79 Published online by Cambridge University Press

J. Cupal, M. A. Drouin, M. Ďurák, B. Himmel, T. Havlíček, P. Homer, A. Honsa, M. Horáček, P. Hríbek, J. Hubáček, Z. Hubka, G. Kalinchenko, K. Kasl, L. Indra, P. Korous, M. Košelja, L. Koubíková, M. Laub, T. Mazanec, A. Meadows, J. Novák, D. Peceli, J. Polan, D. Snopek, V. Šobr, P. Trojek, B. Tykalewicz, P. Velpula, E. Verhagen, Š. Vyhlídka, J. Weiss, C. Haefner, A. Bayramian, S. Betts, A. Erlandson, J. Jarboe, G. Johnson, J. Horner, D. Kim, E. Koh, C. Marshall, D. Mason, E. Sistrunk, D. Smith, T. Spinka, J. Stanley, C. Stolz, T. Suratwala, S. Telford, T. Ditmire, E. Gaul, M. Donovan, C. Frederickson, G. Friedman, D. Hammond, D. Hidinger, G. Chériaux, A. Jochmann, M. Kepler, C. Malato, M. Martinez, T. Metzger, M. Schultze, P. Mason, K. Ertel, A. Lintern, C. Edwards, C. Hernandez-Gomez, and J. Collier. ELI-beamlines: progress in development of next generation short-pulse laser systems. In G. Korn and L. O. Silva, editors, *Proc. SPIE 10241*, page 102410J, 2017.

27. O. Slezák, M. Sawicka-Chyla, M. Divoký, J. Pilař, M. Smrž, and T. Mocek. Thermal-stress-induced birefringence management of complex laser systems by means of polarimetry. *Scientific Reports*, 12(1):18334, Oct. 2022.
28. J. Zhao, Y. Liang, S. Li, Z. Zong, J. Tang, R. Zhao, W. Wang, P. Li, F. Zeng, Y. Xia, L. Chen, B. Chen, K. Zheng, X. Wei, and Q. Zhu. Beam nonuniformity compensating by the programmable spatial shaper for the integration test bed. In A. Tian, editor, *Third International Conference on Photonics and Optical Engineering*, page 140. SPIE, 2019.
29. T. Zhao, J. Yu, C. Li, K. Huang, Y. Ma, X. Tang, and Z. Fan. Beam shaping and compensation for high-gain Nd:glass amplification. *Journal of Modern Optics*, 60(2):109–115, Jan. 2013.

https://doi.org/10.1017/hpl.2023.79 Published online by Cambridge University Press